Electronic Supplementary Material (ESI) for RSC Advances.
This journal is © The Royal Society of Chemistry 2019

Supporting information for

Reverse Monte Carlo Modeling for Local Structures of Noble Metal Nanoparticles Using High-energy XRD and EXAFS

Masafumi Harada,[†] Risa Ikegami,[†] Loku Singgappulige Rosantha Kumara,[‡] Shinji Kohara,[‡] and Osami Sakata* [#]

[†]Department of Health Science and Clothing Environment, Faculty of Human Life and Environment, Nara Women's University, Nara 630-8506, Japan

[‡]Synchrotron X-ray Station at SPring-8, Research Network and Facility Services Division, National Institute for Materials Science (NIMS), 1-1-1 Kouto, Sayo-cho, Sayo-gun, Hyogo, 679-5148, Japan.

[#]Synchrotron X-ray Group, Research Center for Advanced Measurement and Characterization, NIMS, 1-1-1 Kouto, Sayo-cho, Sayo-gun, Hyogo, 679-5148, Japan.

e-mail address: harada@cc.nara-wu.ac.jp (M. Harada).

Table S1. Structural parameters from EXAFS analysis for the metal nanoparticles prepared by the photoreduction in the presence of PVP and benzophenone.

Sample	Edge	Bond	C.N.	r / Å	ΔE / eV	σ^2 / Å^2	R / %[a]
Pt nanoparticles	Pt-L_3	Pt-Pt	8.4	2.75	7.493	0.0066	0.507
Pd nanoparticles	Pd-K	Pd-Pd	9.8	2.75	-1.344	0.0070	0.460
Rh nanoparticles	Rh-K	Rh-Rh	8.1	2.69	-1.353	0.0053	0.495

[a] In the curve fitting process, the goodness of fit (R) by $\{\sum(k^2\chi_{\mathrm{data}}-k^2\chi_{\mathrm{model}})^2\}/\sum(k^2\chi_{\mathrm{data}})^2$ has been estimated with the allowed error range.

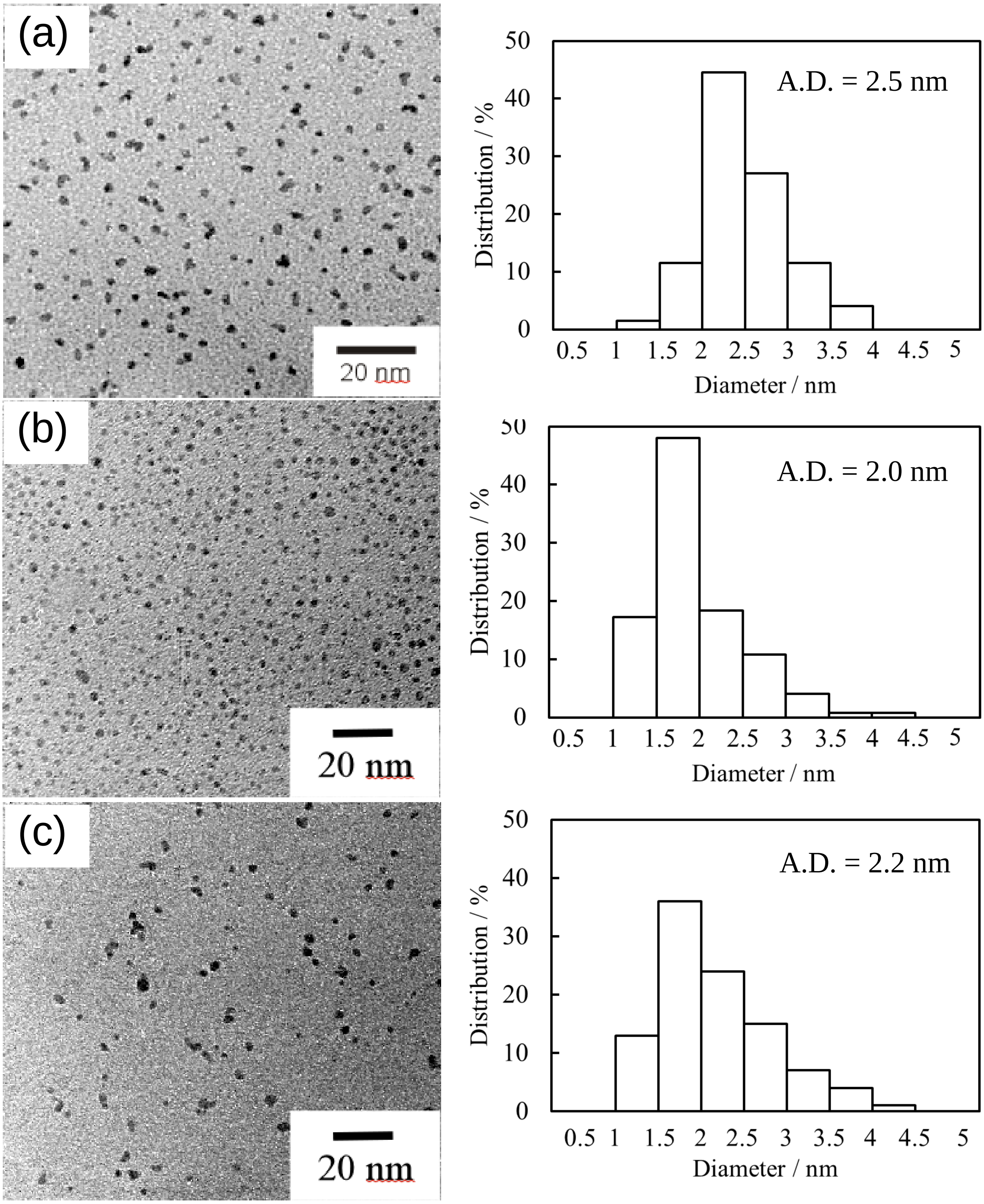

Figure S1. TEM images and particle size distributions of the diameter extracted from the corresponding image for the (a) colloidal dispersions of Pt nanoparticles, (b) colloidal dispersions of Pd nanoparticles, and (c) colloidal dispersions of Rh nanoparticles prepared by the photoreduction in the presence of PVP and benzophenone. Metal concentration in the colloidal dispersions is [Pt] = [Pd] = [Rh] = 24.4 mM. The photoreduction was carried out for 5h.

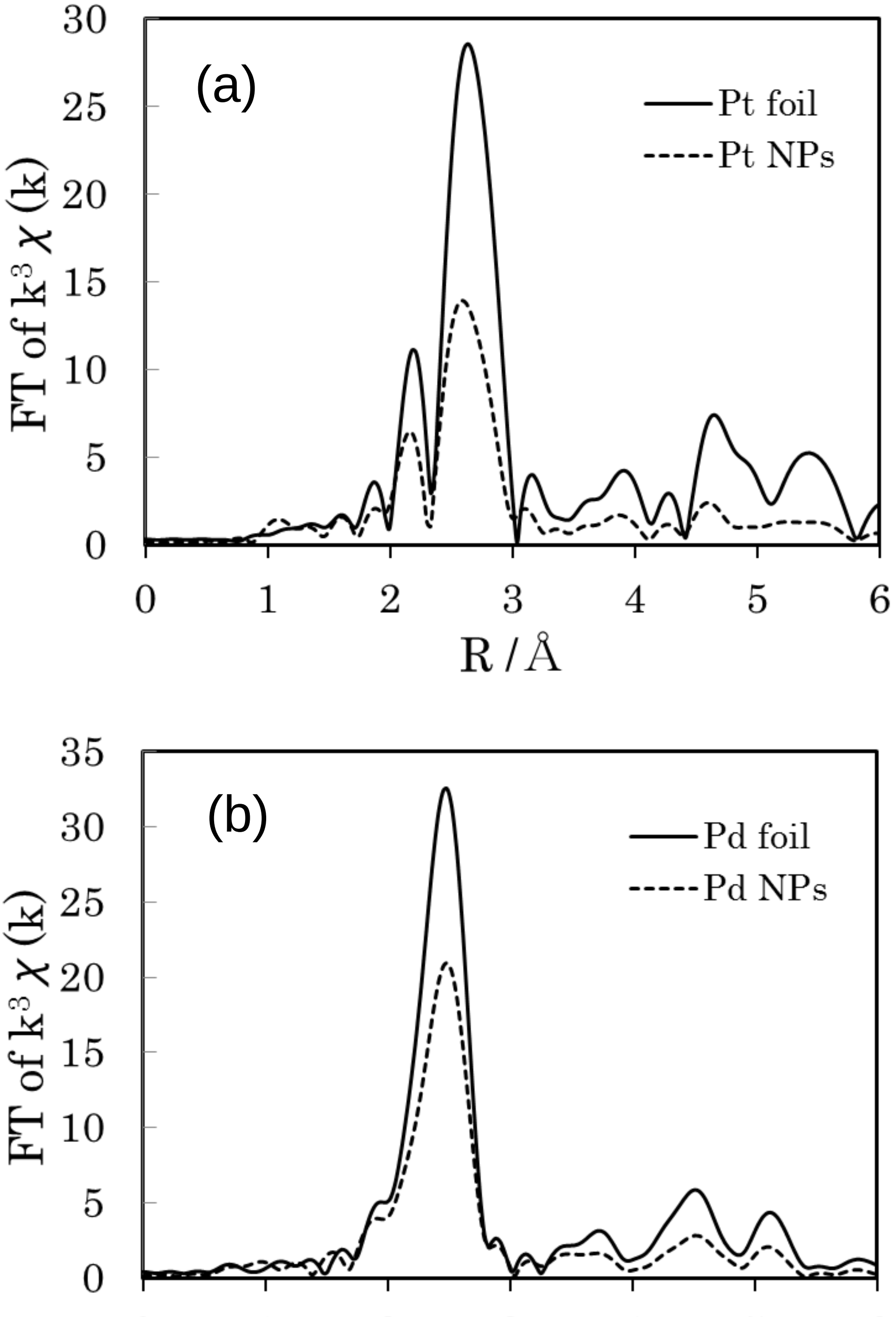
(a)
Pt foil
Pt NPs
FT of $k^3\chi(k)$
30
25
20
15
10
5
0
0
1
2
3
4
5
6
R / Å
(b)
Pd foil
Pd NPs
FT of $k^3\chi(k)$
35
30
25
20
15
10
5
0
0
1
2
3
4
5
6
R / Å

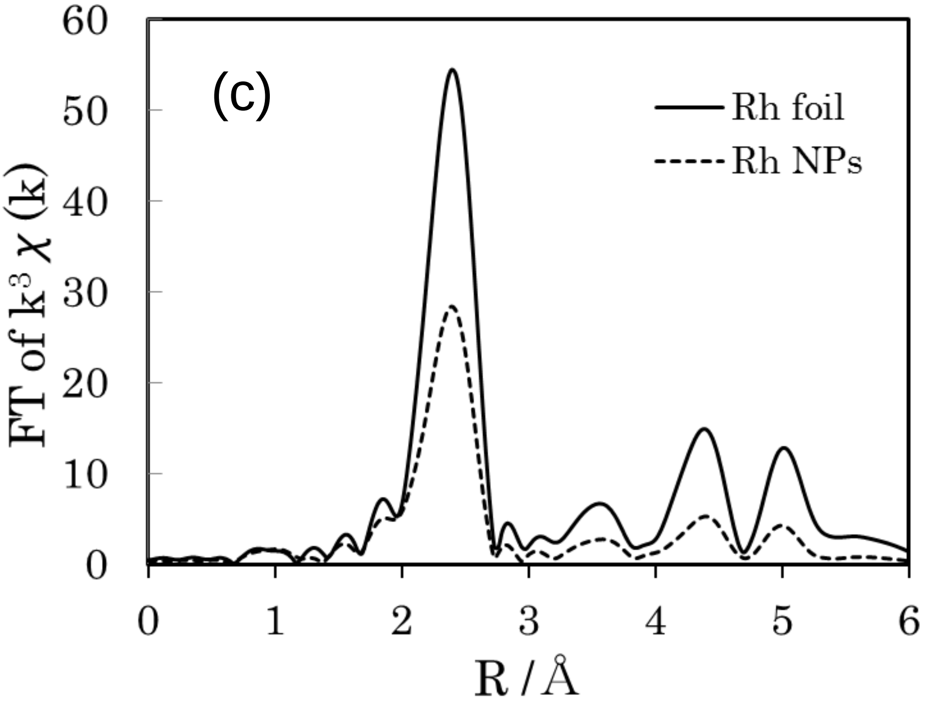

Figure S2. Fourier-transformed $k^3\chi(k)$ EXAFS spectra at the (a) Pt L_3-edge of the Pt foil and Pt nanoparticles, (b) Pd K-edge of the Pd foil and Pd nanoparticles, and (c) Rh K-edge of the Rh foil and Rh nanoparticles.

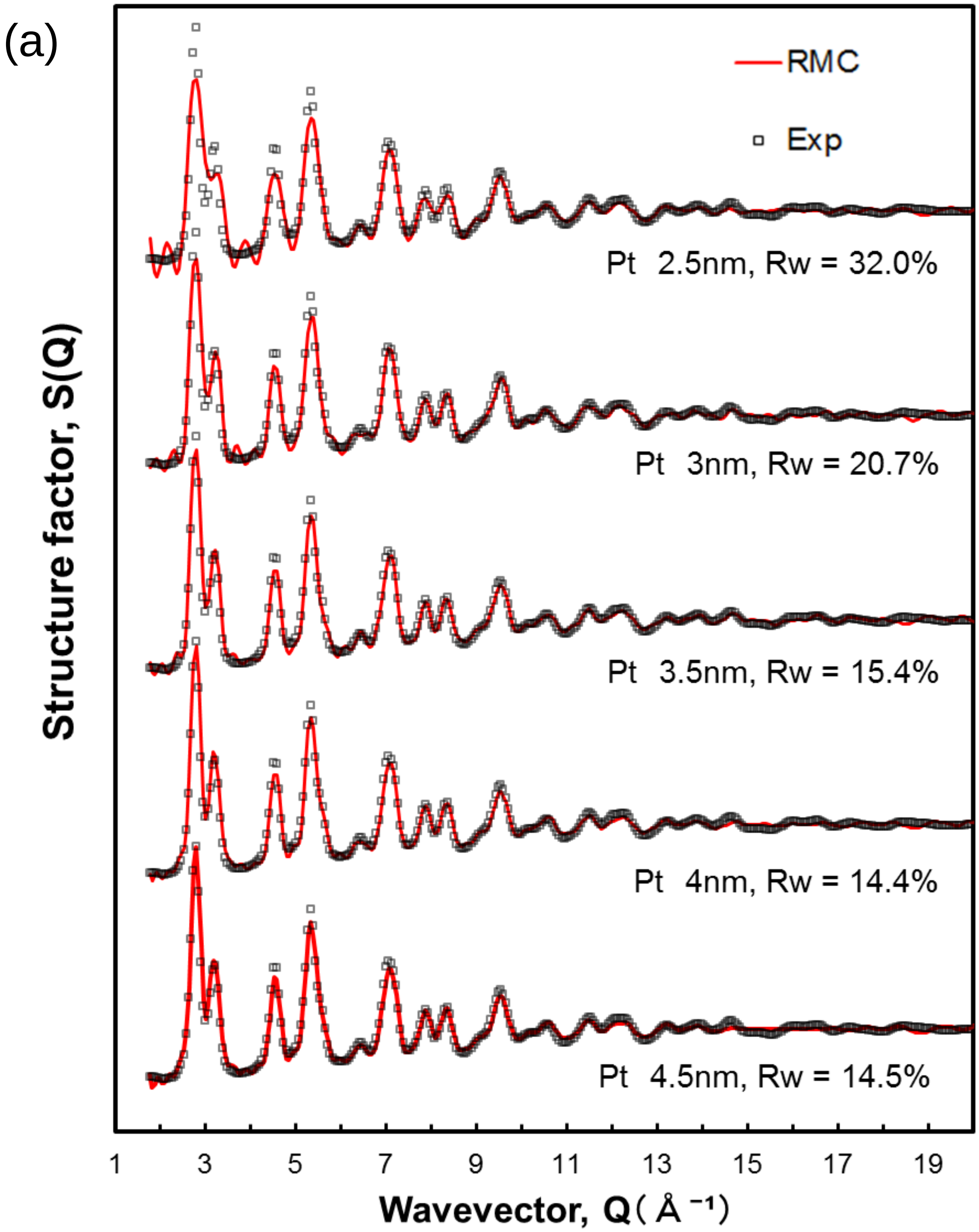
(a)
RMC
Exp
Pt 2.5nm, Rw = 32.0%
Pt 3nm, Rw = 20.7%
Pt 3.5nm, Rw = 15.4%
Pt 4nm, Rw = 14.4%
Pt 4.5nm, Rw = 14.5%
Structure factor, S(Q)
1
3
5
7
9
11
13
15
17
19
Wavevector, Q (Å⁻¹)

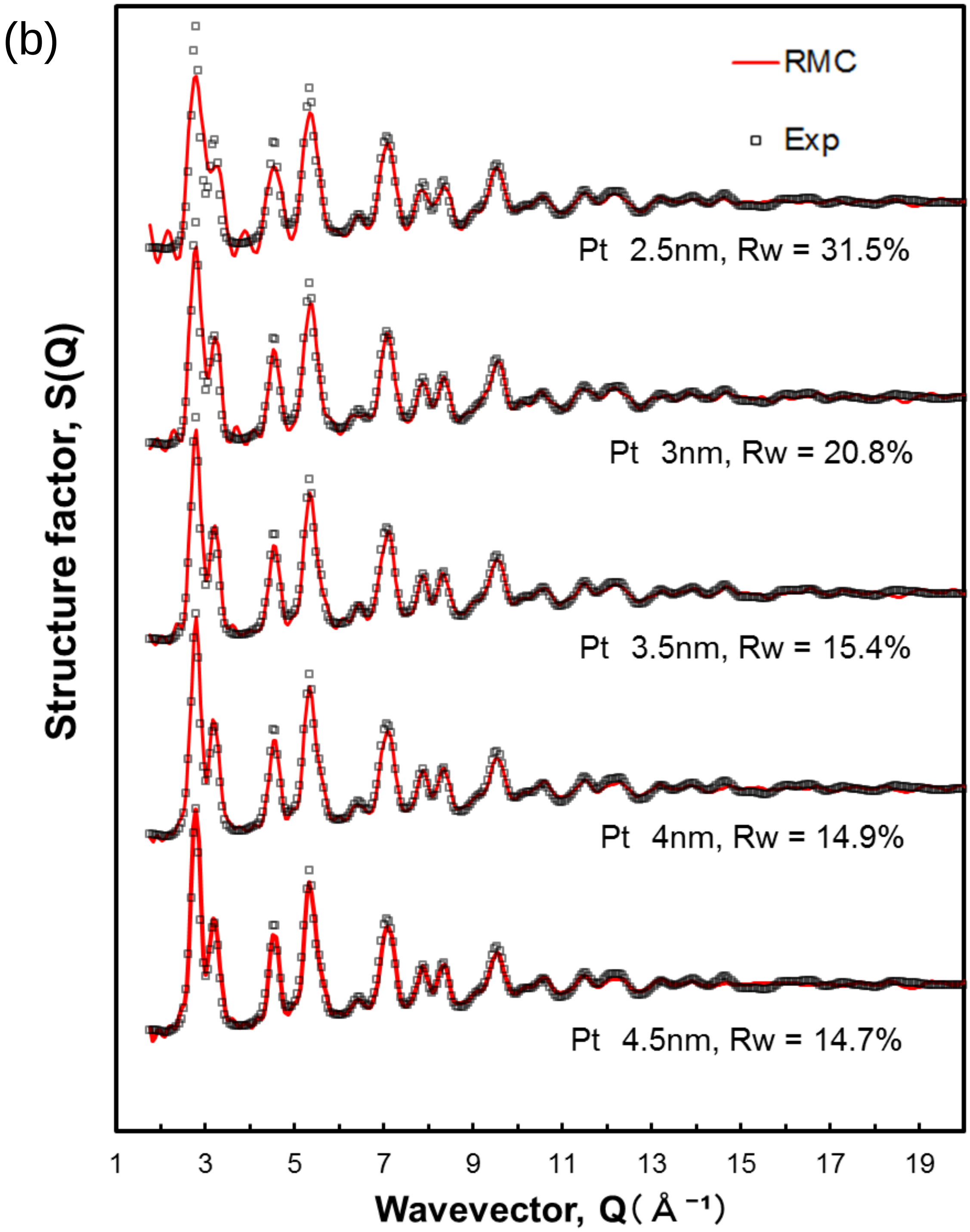

Figure S3. Experimental and RMC-simulated total structure factor *S*(*Q*) profiles for the Pt nanoparticles with different particle sizes ranging from 2.5 to 4.5 nm. The initial configuration for the RMC simulations is based on (a) the fcc bulk Pt crystal structure and (b) the computer-generated random atomic Pt configuration. The black squares represent the experimental total structure factor *S*(*Q*) profiles, and the RMC-simulated total structure factor *S*(*Q*) profiles are shown as red solid lines.

(a)

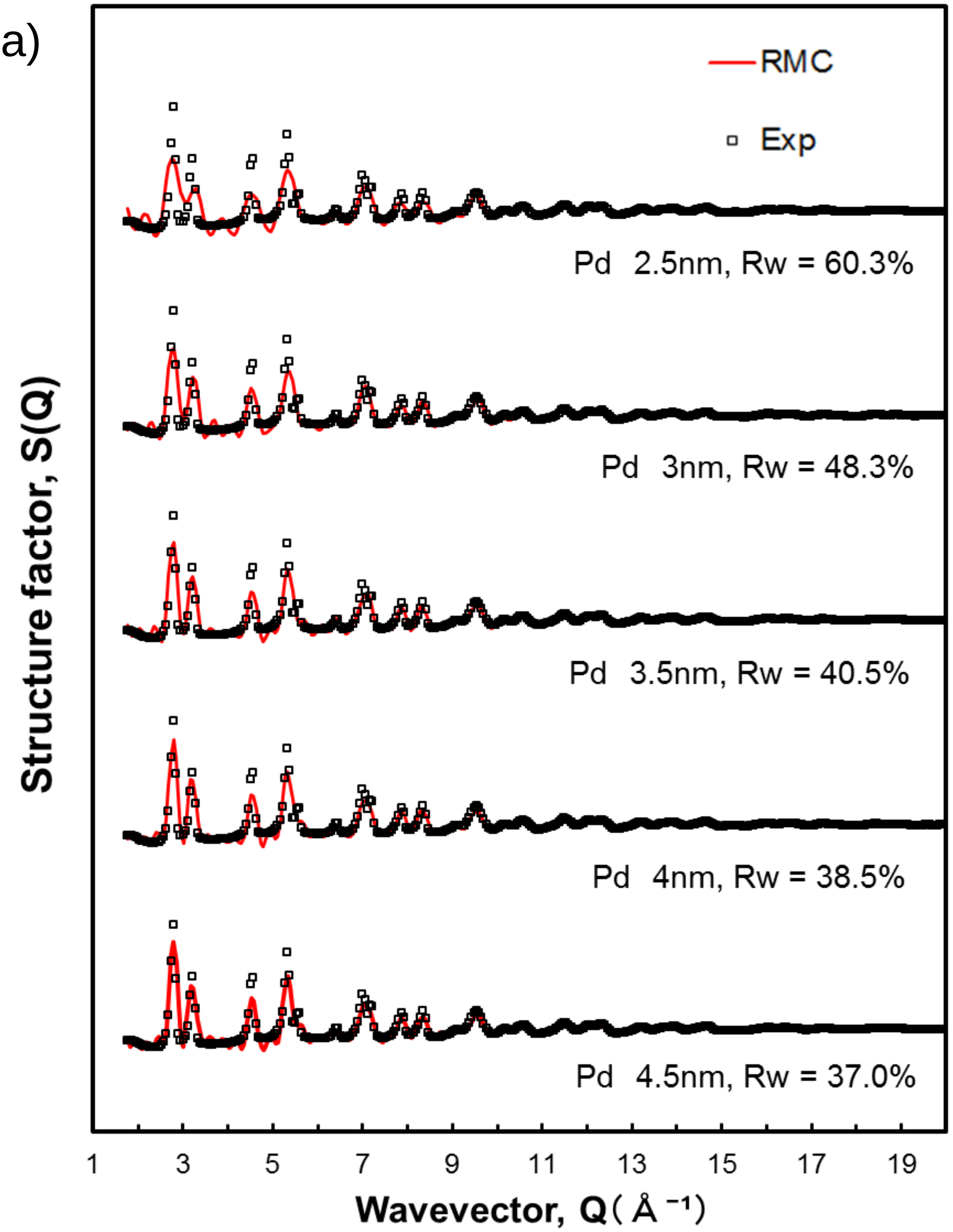
RMC
Exp
Pd 2.5nm, Rw = 60.3%
Pd 3nm, Rw = 48.3%
Pd 3.5nm, Rw = 40.5%
Pd 4nm, Rw = 38.5%
Pd 4.5nm, Rw = 37.0%
Structure factor, S(Q)
1
3
5
7
9
11
13
15
17
19
Wavevector, Q (Å ⁻¹)

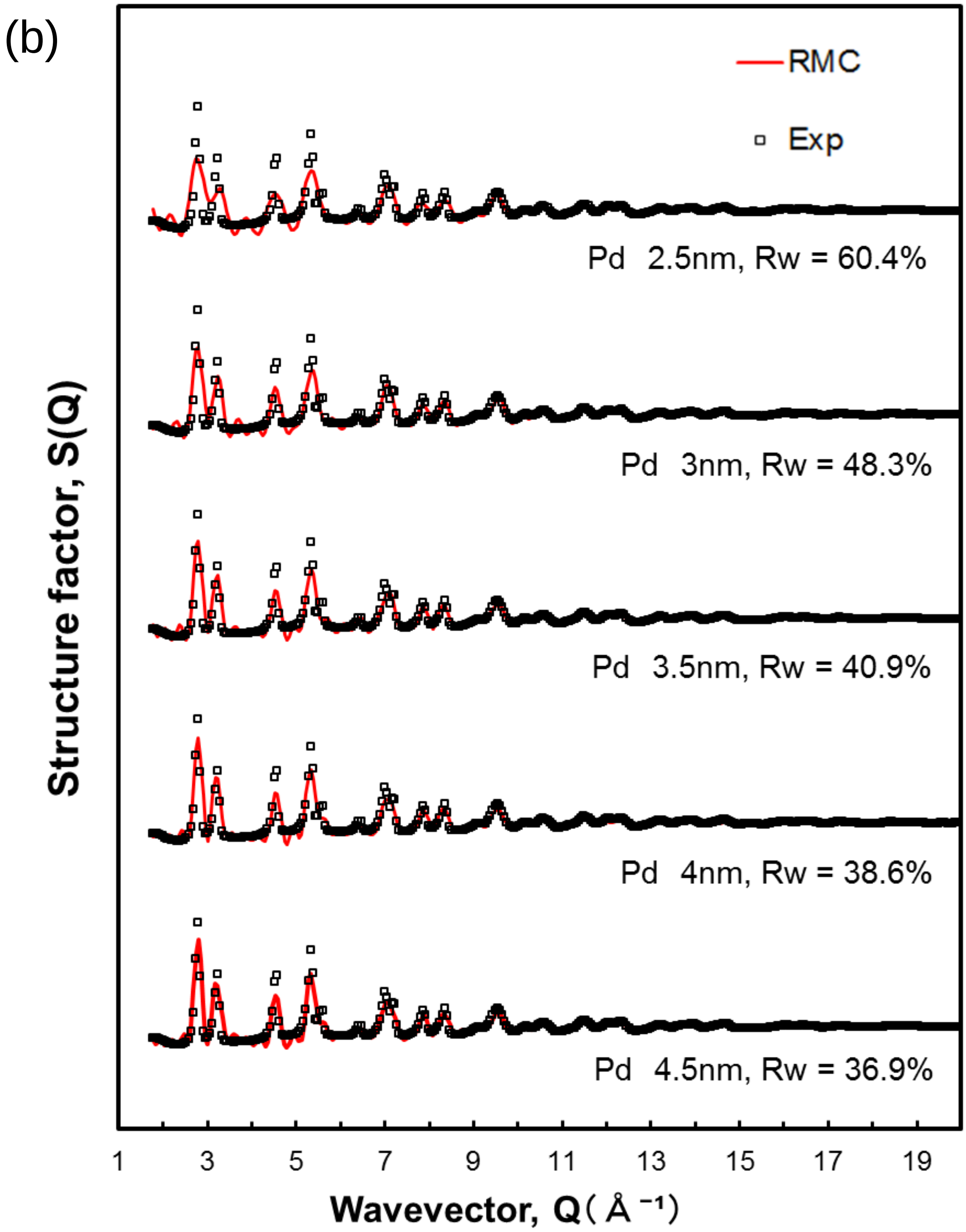

Figure S4. Experimental and RMC-simulated total structure factor $S(Q)$ profiles for the Pd nanoparticles with different particle sizes ranging from 2.5 to 4.5 nm. The initial configuration for the RMC simulations is based on (a) the fcc bulk Pd crystal structure and (b) the computer-generated random atomic Pd configuration. The black squares represent the experimental total structure factor $S(Q)$ profiles, and the RMC-simulated total structure factor $S(Q)$ profiles are shown as red solid lines.

(a)

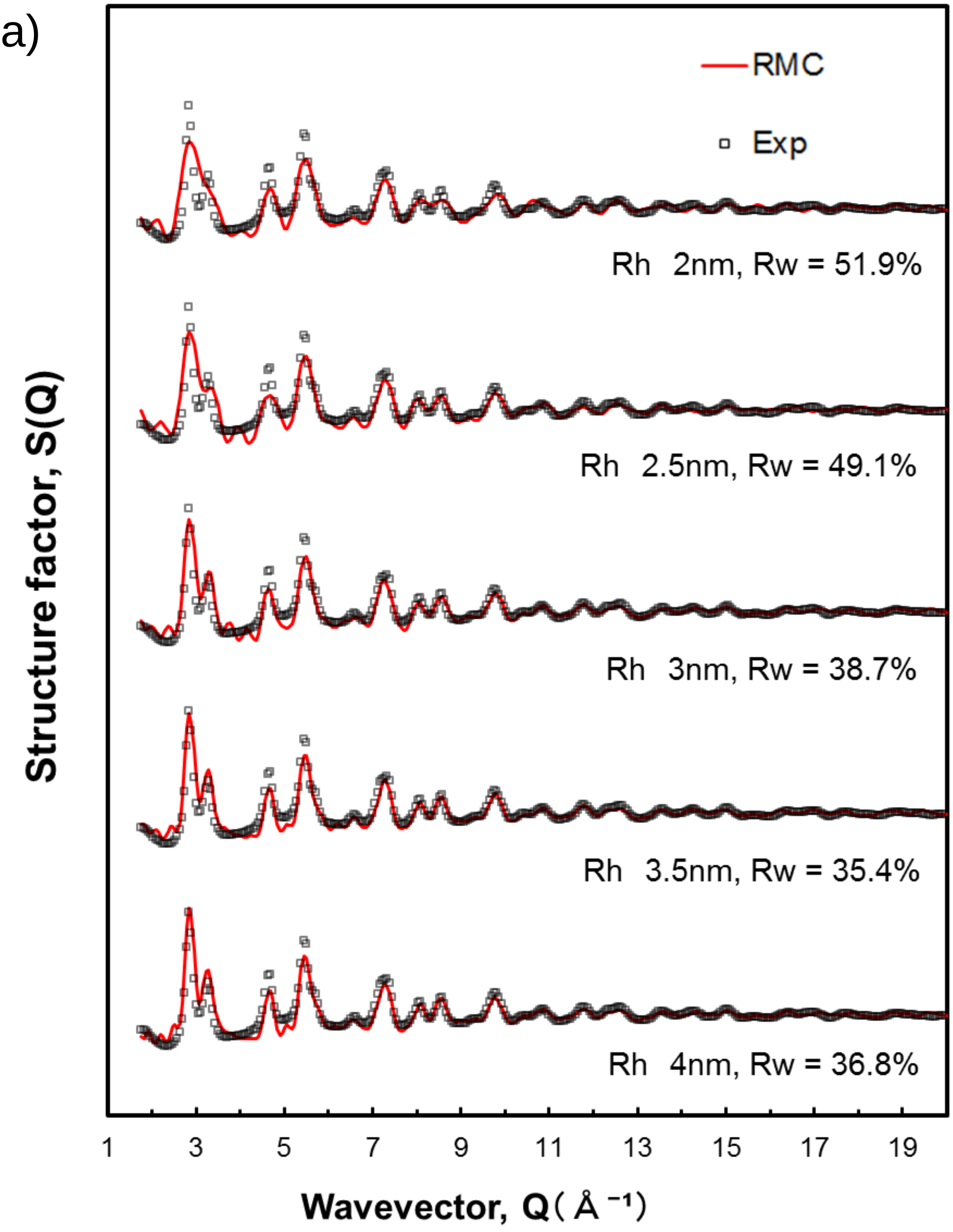
RMC
Exp
Rh 2nm, Rw = 51.9%
Rh 2.5nm, Rw = 49.1%
Rh 3nm, Rw = 38.7%
Rh 3.5nm, Rw = 35.4%
Rh 4nm, Rw = 36.8%
Structure factor, S(Q)
1
3
5
7
9
11
13
15
17
19
Wavevector, Q (Å⁻¹)

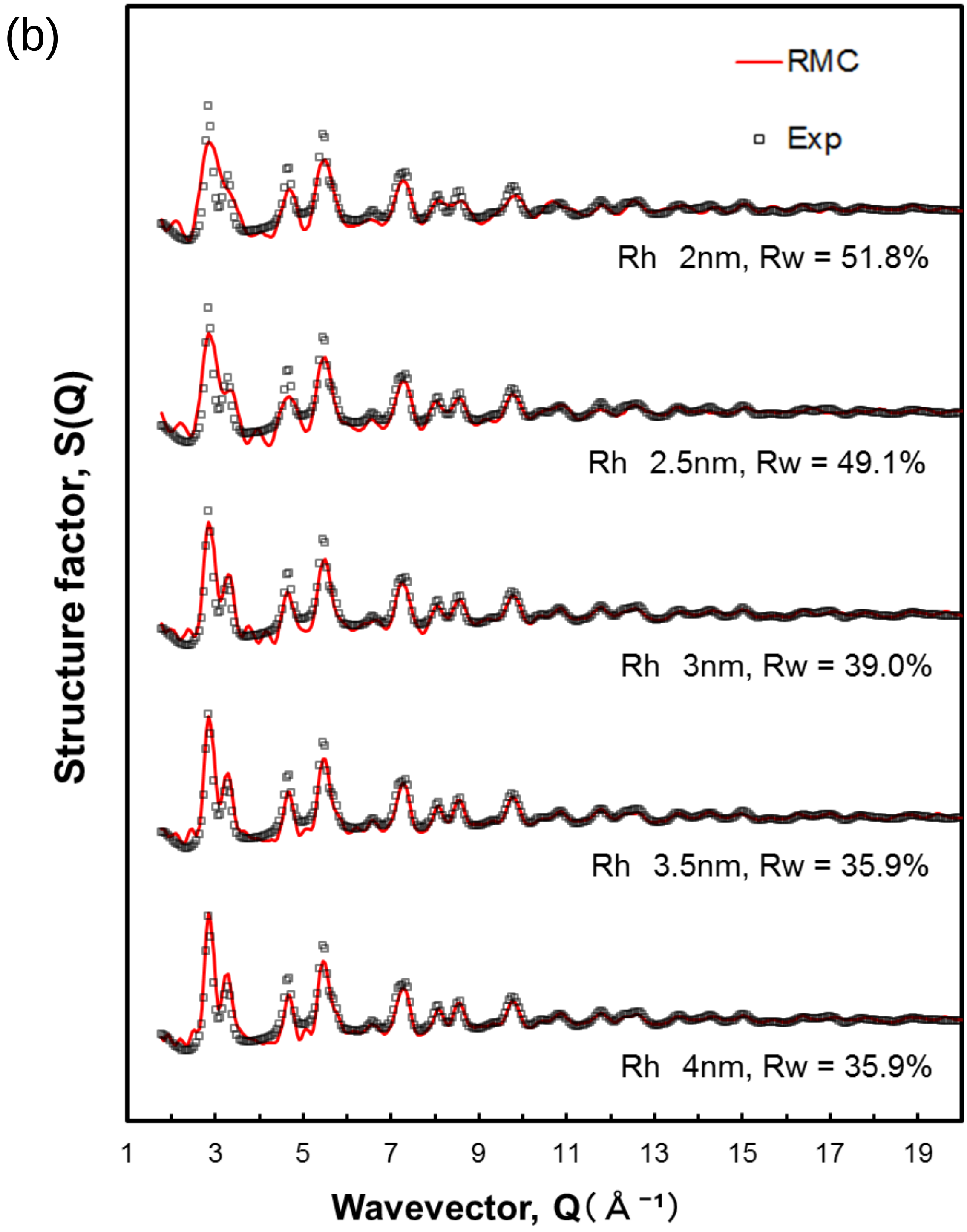

Figure S5. Experimental and RMC-simulated total structure factor *S*(*Q*) profiles for the Rh nanoparticles with different particle sizes ranging from 2.0 to 4.0 nm. The initial configuration for the RMC simulations is based on (a) the fcc bulk Rh crystal structure and (b) the computer-generated random atomic Rh configuration. The black squares represent the experimental total structure factor *S*(*Q*) profiles, and the RMC-simulated total structure factor *S*(*Q*) profiles are shown as red solid lines.

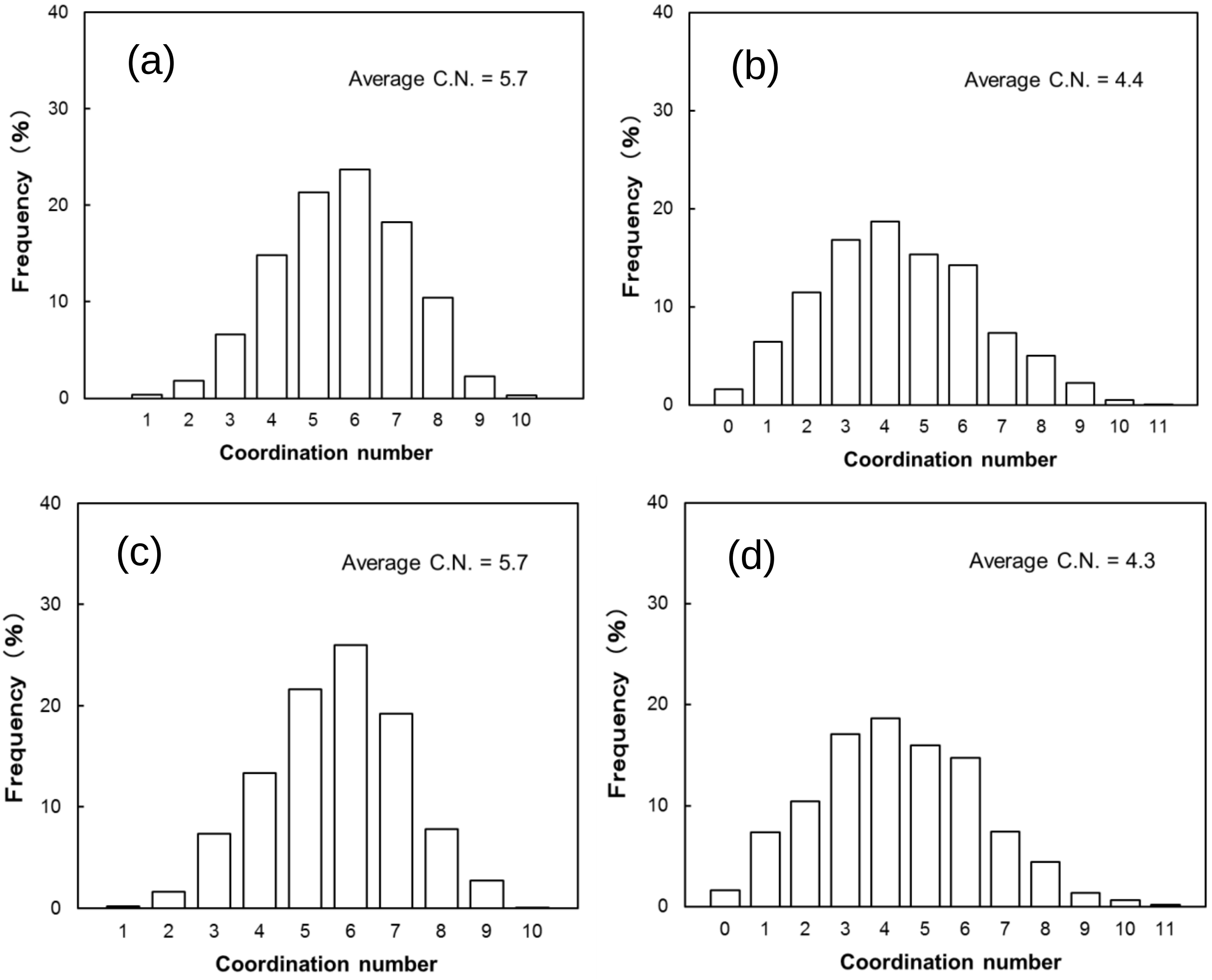

Figure S6. Distributions of the coordination numbers (C.N.s) in the first and second coordination shell for the 3.5 nm Pt nanoparticles. The distributions are extracted from the RMC-generated structure models (as shown in Figure 5(a)) by the analysis of PDFs data. The initial configuration for the RMC simulations is based on (a and b) the fcc bulk crystal structure and (c and d) the computer-generated random atomic configurations. (a and c): the first coordination shell, and (b and d): the second coordination shell.

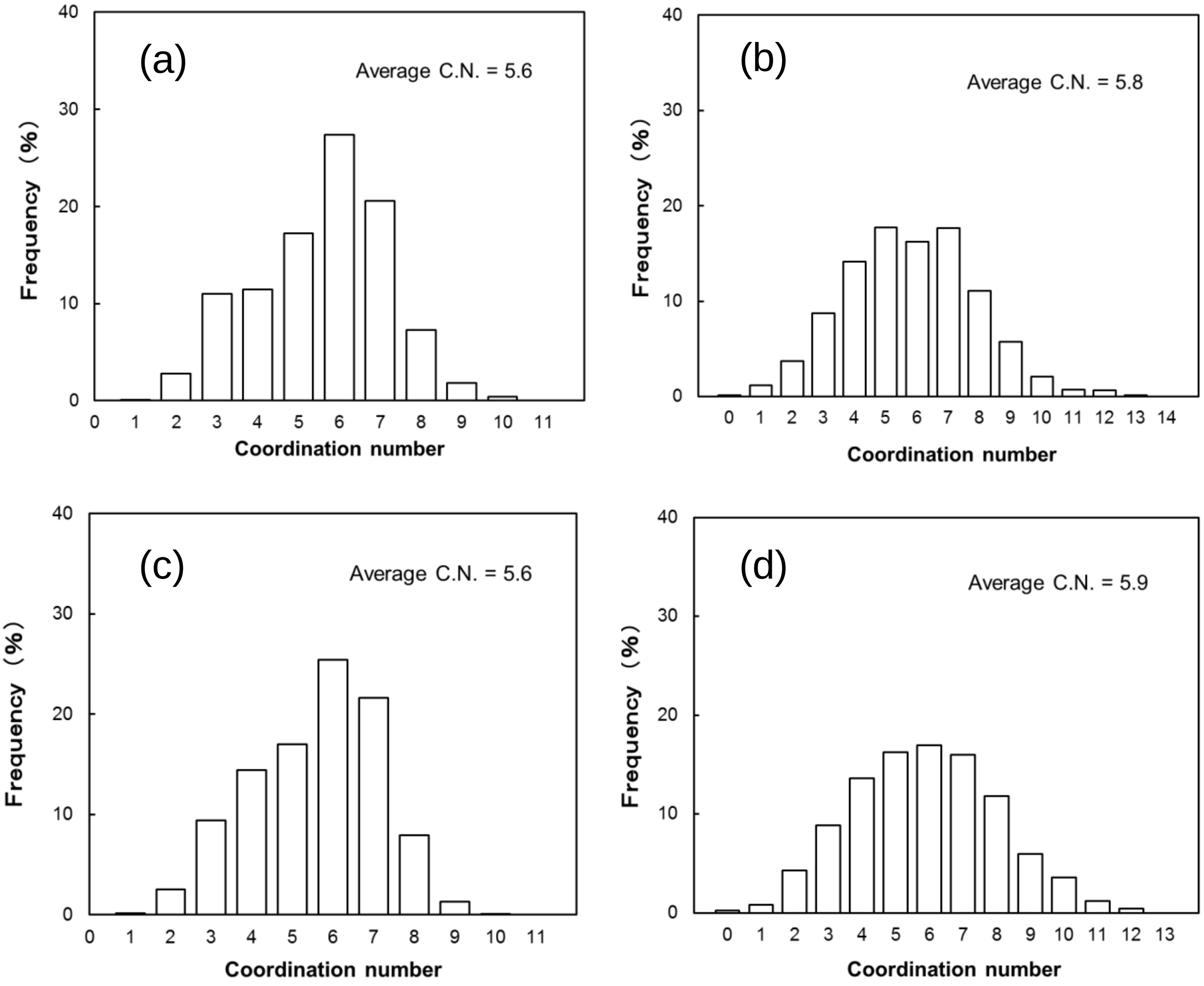

Figure S7. Distributions of the coordination numbers (C.N.s) in the first and second coordination shell for the 4.0 nm Pd nanoparticles. The distributions are extracted from the RMC-generated structure models (as shown in Figure 5(b)) by the analysis of PDFs data. The initial configuration for the RMC simulations is based on (a and b) the fcc bulk crystal structure and (c and d) the computer-generated random atomic configurations. (a and c): the first coordination shell, and (b and d): the second coordination shell.

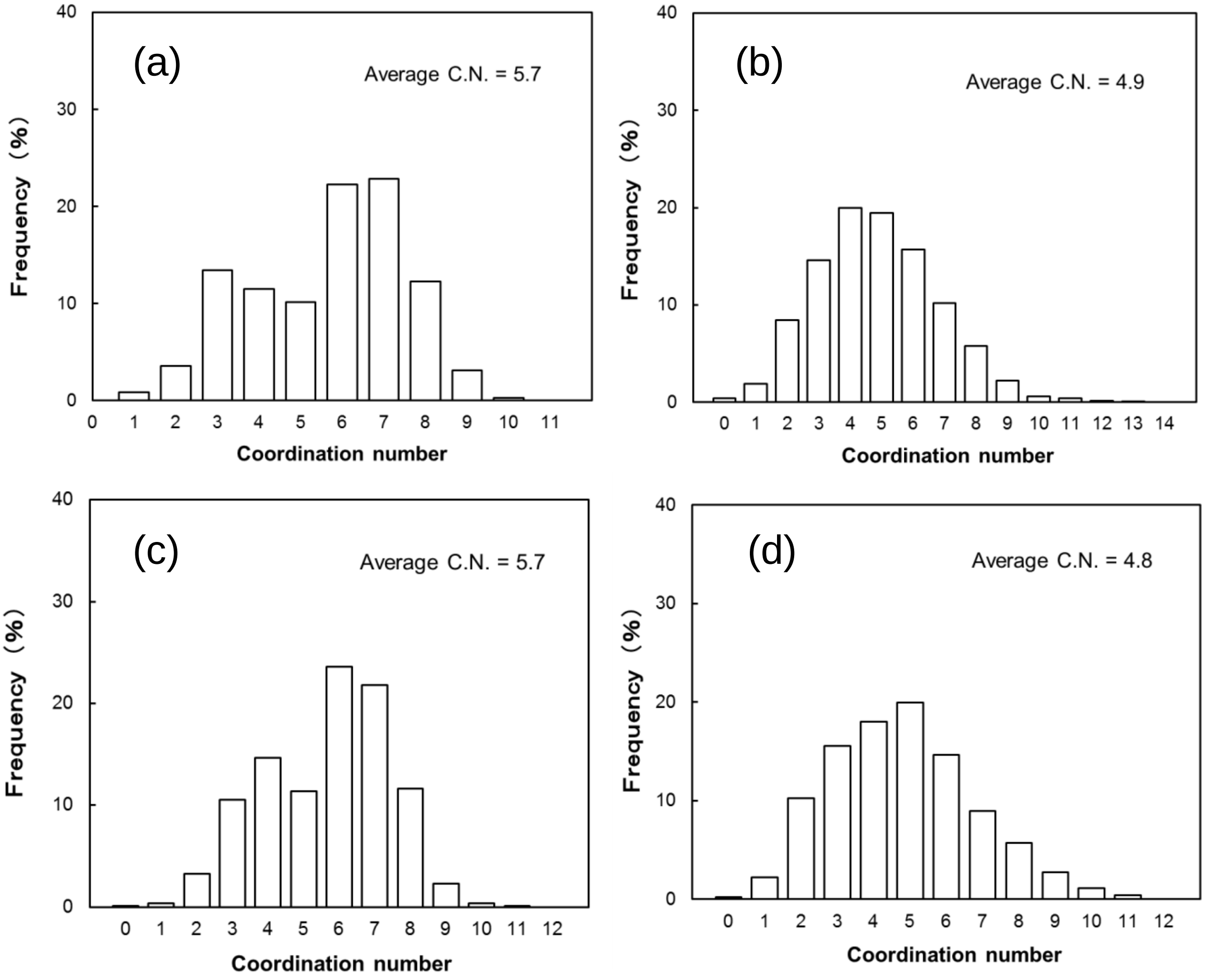

Figure S8. Distributions of the coordination numbers (C.N.s) in the first and second coordination shell for the 3.5 nm Rh nanoparticles. The distributions are extracted from the RMC-generated structure models (as shown in Figure 5(c)) by the analysis of PDFs data. The initial configuration for the RMC simulations is based on (a and b) the fcc bulk crystal structure and (c and d) the computer-generated random atomic configurations. (a and c): the first coordination shell, and (b and d): the second coordination shell.

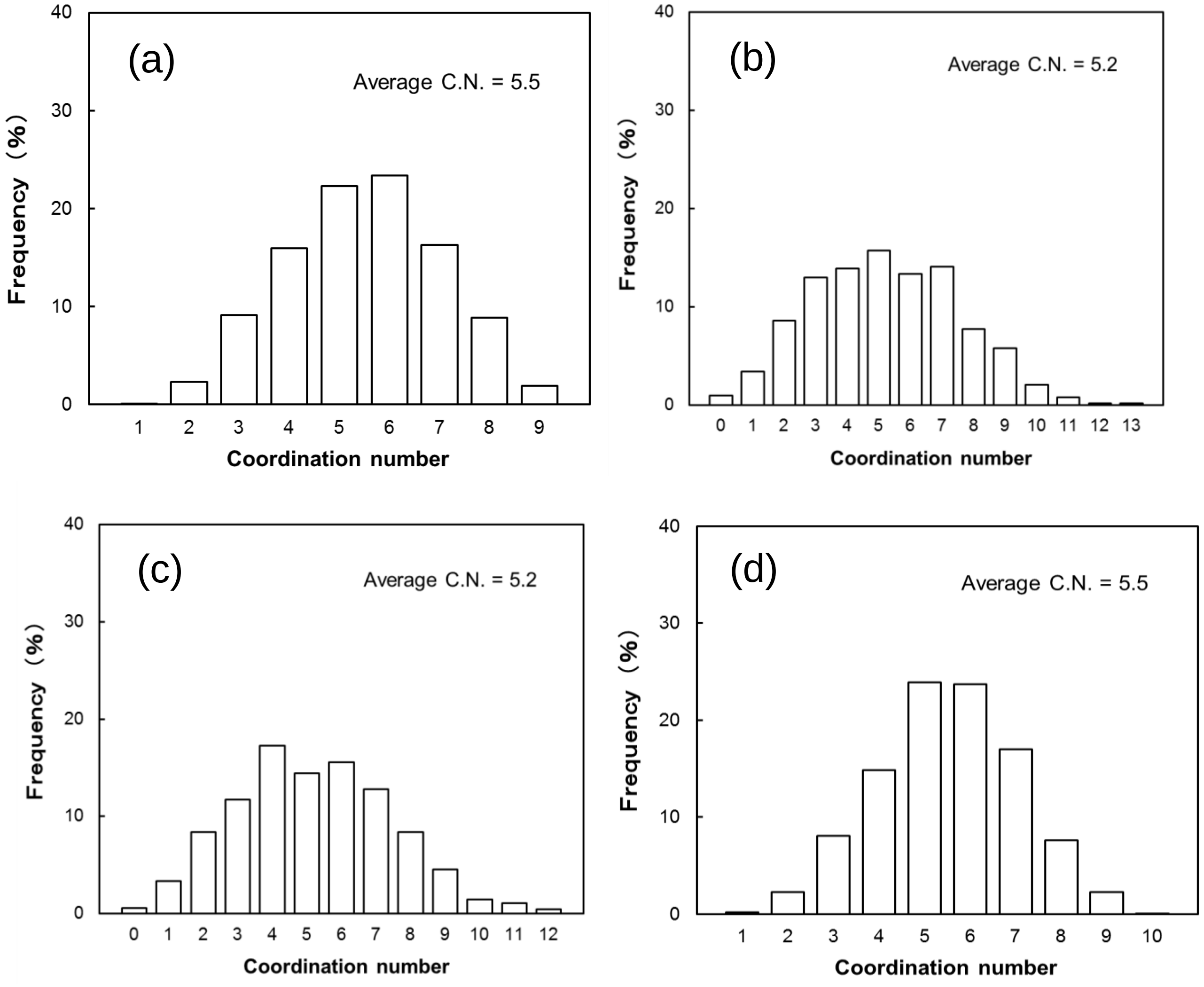

Figure S9. Distributions of the coordination numbers (C.N.s) in the first and second coordination shell for the 3.5 nm Pt nanoparticles. The distributions are extracted from the RMC-generated structure models (as shown in Figure 5(a)) by the analysis of EXAFS data shown in Figure 7(a) and 7(b). The initial configuration for the RMC simulations is based on (a and b) the fcc bulk crystal structure and (c and d) the computer-generated random atomic configurations. (a and c): the first coordination shell, and (b and d): the second coordination shell.

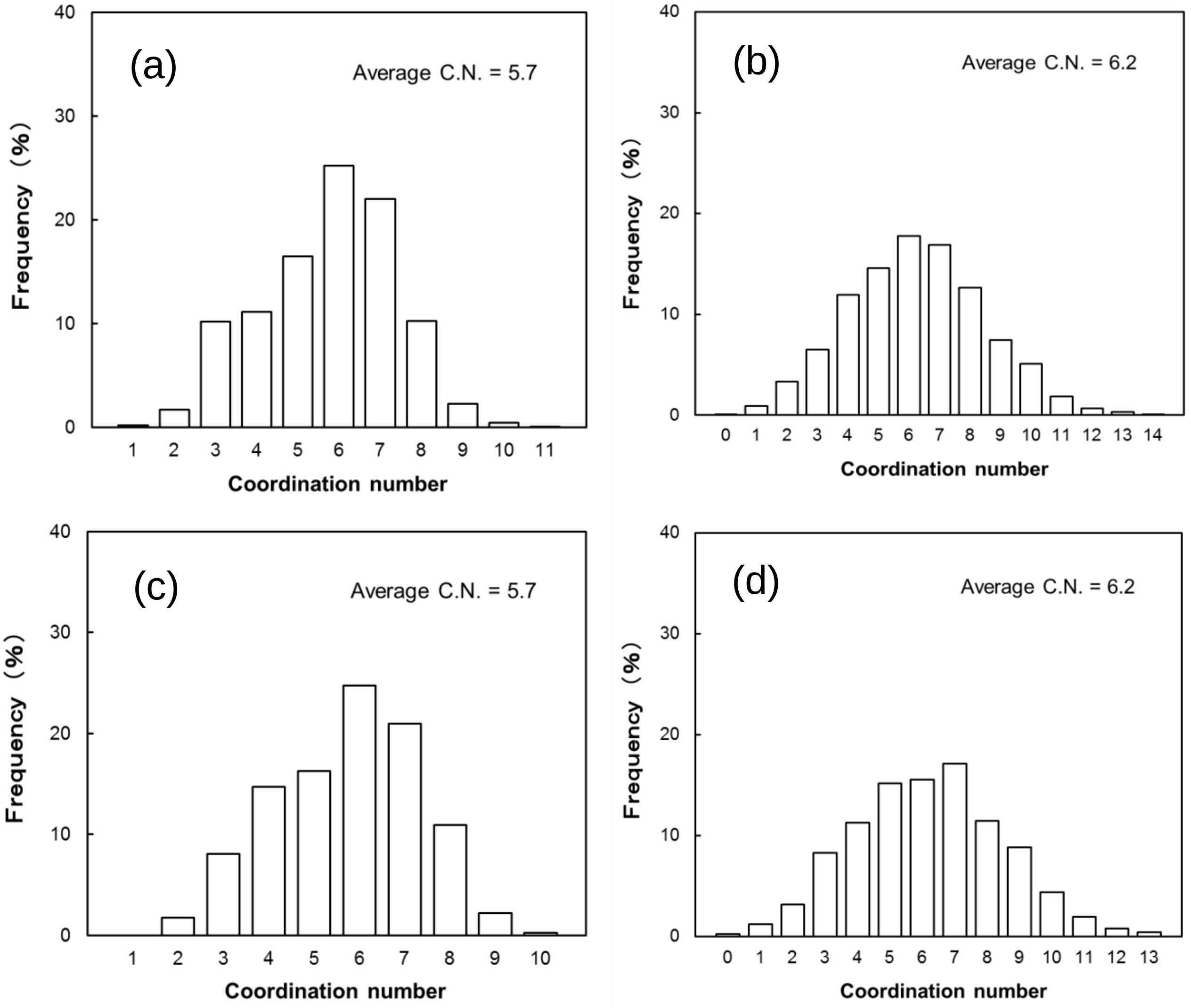

Figure S10. Distributions of the coordination numbers (C.N.s) in the first and second coordination shell for the 4.0 nm Pd nanoparticles. The distributions are extracted from the RMC-generated structure models (as shown in Figure 5(b)) by the analysis of EXAFS data shown in Figure 7(c) and 7(d). The initial configuration for the RMC simulations is based on (a and b) the fcc bulk crystal structure and (c and d) the computer-generated random atomic configurations. (a and c): the first coordination shell, and (b and d): the second coordination shell.

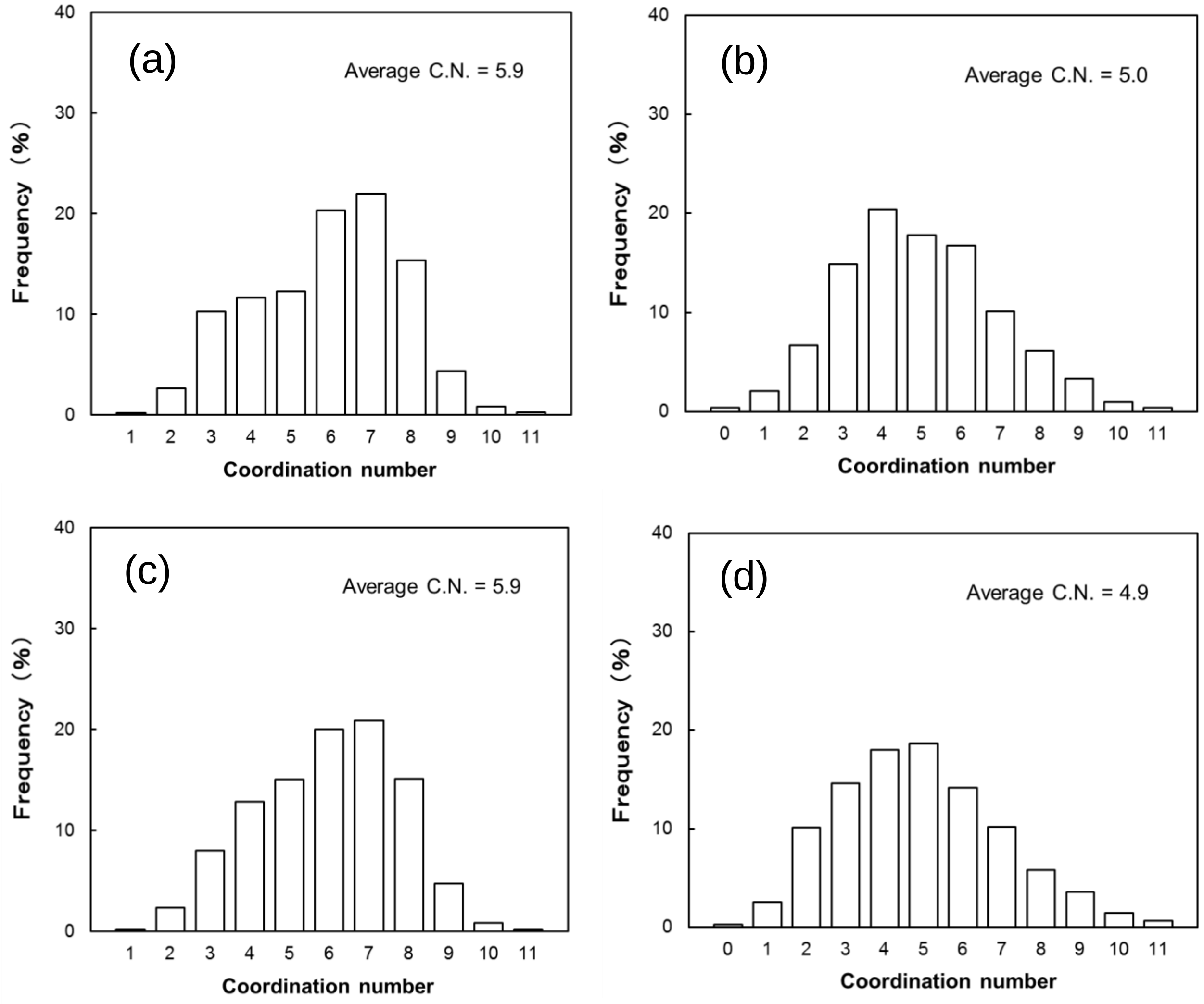

Figure S11. Distributions of the coordination numbers (C.N.s) in the first and second coordination shell for the 3.5 nm Rh nanoparticles. The distributions are extracted from the RMC-generated structure models (as shown in Figure 5(c)) by the analysis of EXAFS data shown in Figure 7(e) and 7(f). The initial configuration for the RMC simulations is based on (a and b) the fcc bulk crystal structure and (c and d) the computer-generated random atomic configurations. (a and c): the first coordination shell, and (b and d): the second coordination shell.

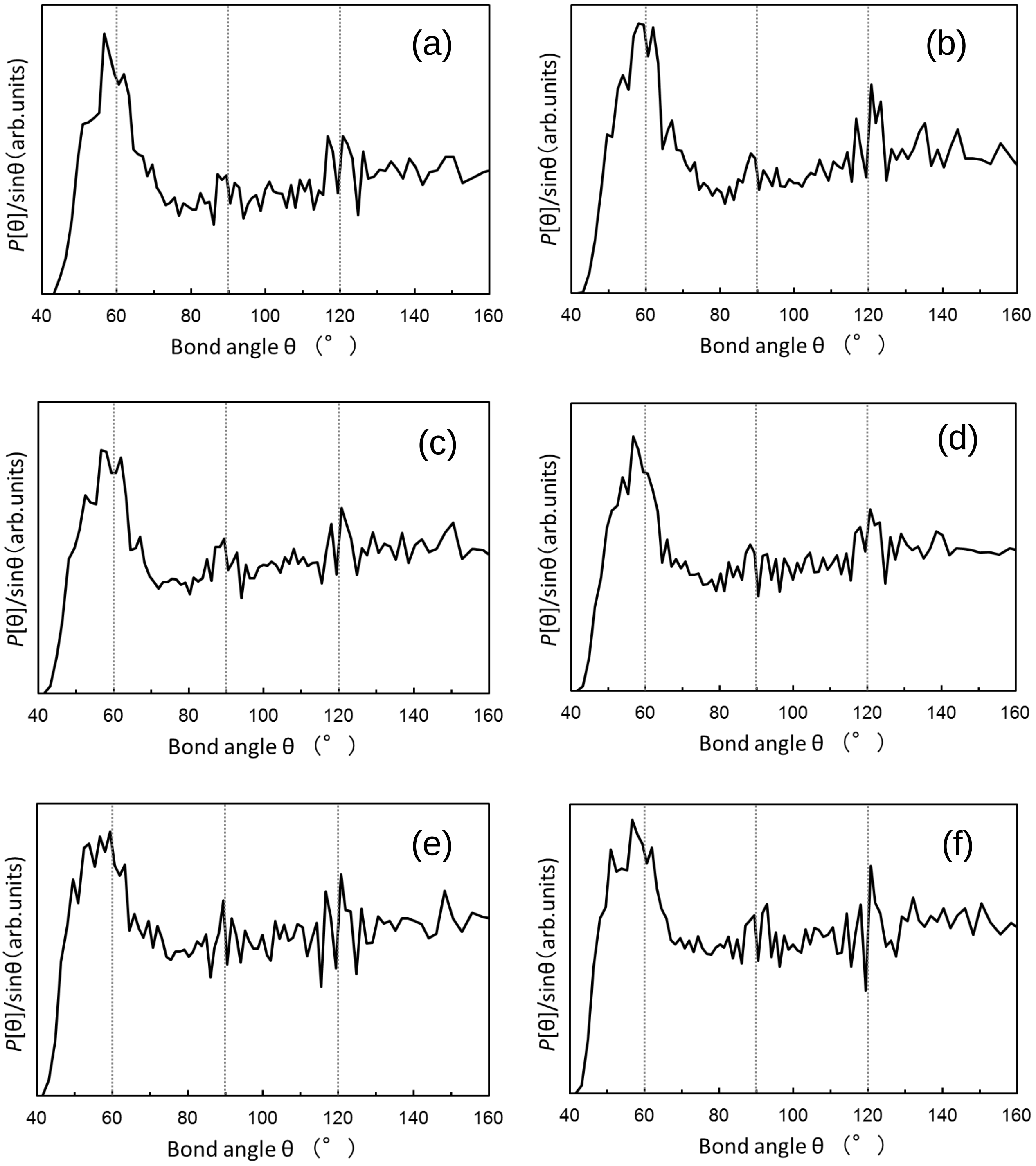

Figure S12. Distribution of bond angles derived from the RMC simulations by the analysis of EXAFS data for the 3.5 nm Pt nanoparticles, 4.0 nm Pd nanoparticles, and 3.5 nm Rh nanoparticles. The initial configuration for the RMC simulations is based on (a, c, and e) the fcc bulk crystal structure and (b, d, and f) the computer-generated random atomic configuration for the respective nanoparticles. (a and b): Pt nanoparticles, (c and d): Pd nanoparticles, and (e and f): Rh nanoparticles.